ATMOSPHERIC SCIENCE

Substantial global influence of anthropogenic aerosols on tropical cyclones over the past 40 years

Hiroyuki Murakami[1,2]*

Over the past 40 years, anthropogenic aerosols have been substantially decreasing over Europe and the United States owing to pollution control measures, whereas they have increased in South and East Asia because of the economic and industrial growth in these regions. However, it is not yet clear how the changes in anthropogenic aerosols have altered global tropical cyclone (TC) activity. In this study, we reveal that the decreases in aerosols over Europe and the United States have contributed to significant decreases in TCs over the Southern Hemisphere as well as increases in TCs over the North Atlantic, whereas the increases in aerosols in South and East Asia have exerted substantial decreases in TCs over the western North Pacific. These results suggest that how society controls future emissions of anthropogenic aerosols will exert a substantial impact on the world's TC activity.

INTRODUCTION

The effect of anthropogenic climate change on global tropical cyclone (TC) activity is of great interest for society because of the substantial adverse impacts that TCs can have in terms of natural hazards, water resources, ecosystems, economies, insurance, and mitigation policy. Hence, a large body of work has already been carried out by scientists with respect to how anthropogenic climate changes can potentially alter global TC activity, and this has been examined in the context of past, present-day, and future climates (1, 2). Although the detection and attribution of changes in TC activity in the past is a challenging topic owing to the lack of long-term reliable observations, several studies have shown a potential impact of anthropogenic climate changes on global TC activity over the past 40 years (1–6). Specifically, Murakami et al. (5) revealed, using a large number of climate modeling simulations, that a climatological change in global TC activity over the period 1980–2018 can be detected in the spatial pattern of TC frequency of occurrence (i.e., TCF or TC density; "Observed data" section). They showed that TCF has decreased substantially in the South Indian Ocean and western North Pacific (WNP) since 1980, whereas it has increased in the North Atlantic (NA) and Central Pacific. They revealed that these changes were attributable to the changes in combined external forcing, including greenhouse gases, anthropogenic aerosols, and volcanic eruptions.

Meanwhile, Murakami et al. (5) showed substantial decreases in TCF over the NA in the experiments in which only CO_2 was increased while other external forcings were fixed. The sign of the changes in TCF in the NA was opposite to that in the experiments run with all anthropogenic forcings. These results indicate a substantial influence of anthropogenic aerosols on TC activity in the NA, which is a finding that is consistent with a previous study (7). Evan et al. (8) also reported a potential impact of anthropogenic aerosols from South Asia on TC activity over the Arabian Sea. However, these studies focused on the impacts of aerosols on TC activity at local scale. There is relatively less literature on how the changes in anthropogenic aerosols all over the world could have potentially influenced global TC activity over the past 40 years. Emissions of anthropogenic aerosols, specifically sulfate, since 1980 have been spatially inhomogeneous, with decreased levels in the Western Hemisphere (e.g., Europe and the United States) owing to pollution control measures and increased levels in the Eastern Hemisphere (e.g., South and East Asia) because of the economic and industrial growth in these regions. We hypothesize that this spatial contrast in the changes in aerosol emissions may have had substantial impacts on TC activity not only at local scales but also at the global scale, through global changes in large-scale circulation patterns. By analyzing the results from several idealized climate simulations, the present paper reveals how the global changes in emissions of anthropogenic aerosols since 1980 may have influenced the spatial distributions of TCs throughout the world.

RESULTS

Changes in TC spatial distributions

Figure 1A shows the observed difference in TCF ("Observed data" section) between the means of 2001–2020 and 1980–2000, revealing significant decreases in TCF over the WNP and Southern Hemisphere (SH) and increases in the NA (highlighted in the black rectangles in Fig. 1A). The observed changes in sea surface temperature (SST) over the same period show substantial warming globally (Fig. 1B). Specifically, the warming is larger over the mid-latitudes of the WNP, NA, and southern Pacific. The east-west spatial contrast in the warming over the Pacific Ocean, with a triangular-shaped cooling region in the east, resembles the known patterns of decadal variation in SSTs [e.g., mega El Niño–Southern Oscillation (9) or Interdecadal Pacific Oscillation (10)] such that the observed changes in TCF, as shown in Fig. 1A, could be a result of various factors including multidecadal internal variation and/or anthropogenic forcing such as greenhouse gases and aerosols, as reviewed by Murakami et al. (5).

To reveal the individual impacts of the regional distribution of changes in anthropogenic aerosols on TCs globally since 1980, we conducted idealized climate model experiments by imposing different spatial emission patterns of anthropogenic aerosols (including sulfate, black carbon, and organic carbon aerosols related to human activity), while the other experimental settings remained identical ("Model" and "Model experiments" sections). In the early-decade

[1]National Oceanic and Atmospheric Administration/Geophysical Fluid Dynamics Laboratory, Princeton, NJ, USA. [2]University Corporation for Atmospheric Research, Boulder, CO, USA.
*Corresponding author. Email: hir.murakami@gmail.com
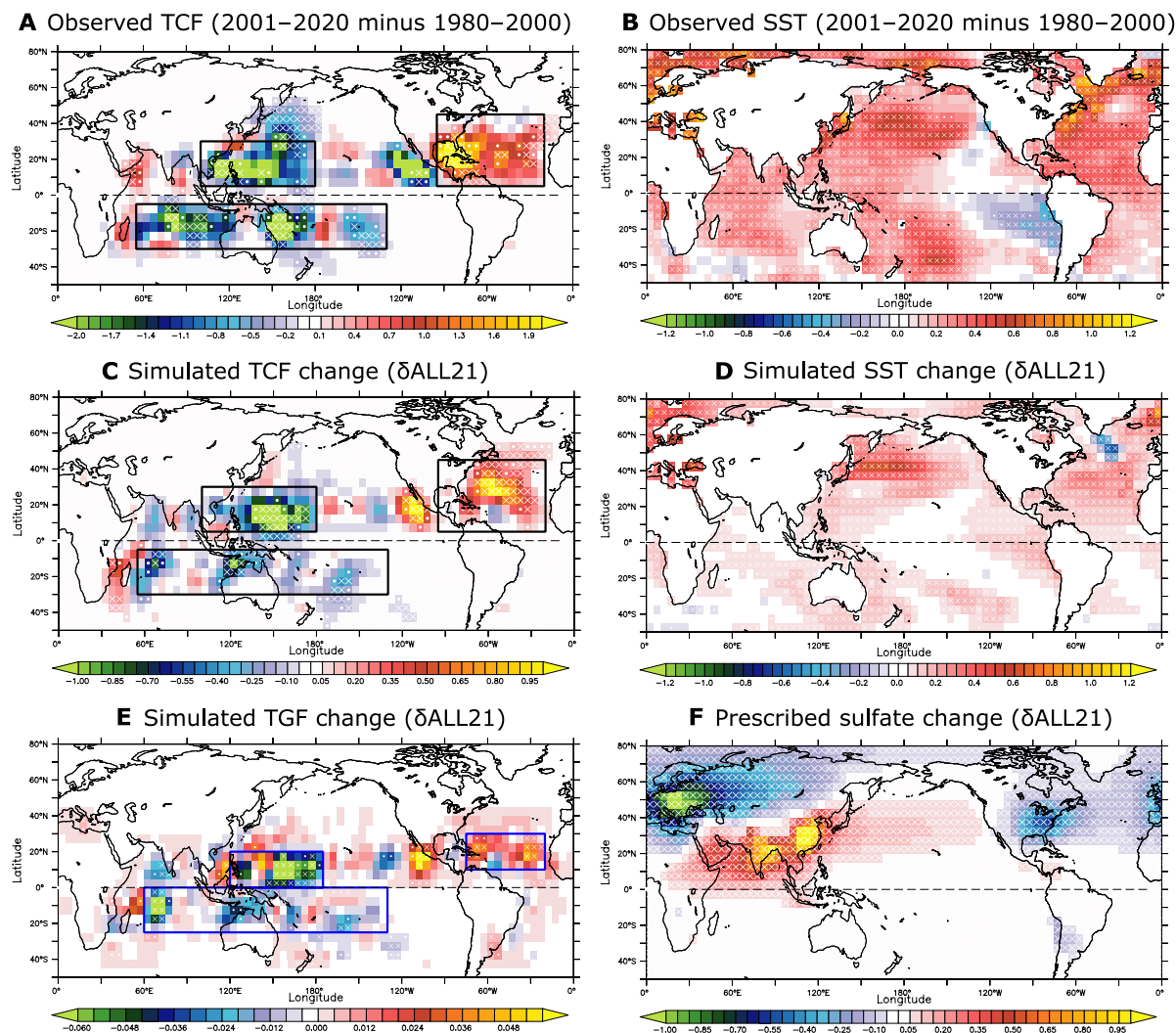
Fig. 1. Observed and simulated changes in SST, TCF, TGF, and sulfate. (**A**) Mean difference in the observed (A) TCF and (**B**) SST between 1980–2000 and 2001–2020. (**C** and **D**) As in (A) and (B) but for the simulated differences between ALL21 and CNTL. (**E** and **F**) As in (C) but for the simulated TGF and simulated column-integrated sulfate burden in response to the prescribed emissions of sulfate, respectively. Note that sulfate aerosols are just one type of aerosol emission included in the experiments, along with black carbon and organic carbon. White crosses (dots) indicate where the difference over the grid cell is statistically significant at the 95% (90%) level according to the bootstrap method. Units: number per year for TCF and TGF, K for SST, and kg m^{-2} for sulfate.

control experiment (CNTL), the mean emissions of anthropogenic aerosols for the period 1980–2000 were prescribed, whereas the mean values during 2001–2020 were adopted in the late-decade experiment (ALL21). The difference in the simulated sulfate aerosols between ALL21 and CNTL—namely, δALL21—is shown in Fig. 1F, revealing substantial decreases in anthropogenic sulfates over Europe and the United States and increases over South and East Asia. The resultant differences in the simulated TCF and SST reveal somewhat similar spatial patterns as observed, especially over the domains of interest (Fig. 1, C and D). These consistent changes in TCF and SST between observations and the model simulations reveal a substantial influence of anthropogenic aerosols on the global distribution of TCs and associated large-scale parameters.

The changes in TCF might be associated with the corresponding changes in TC genesis frequency (dg), TC track or motion (dt), and/or their nonlinear combinations (dn). We applied an empirical statistical method of passage frequency (*11*, *12*) ("Empirical statistical

analysis for TCs" section) to quantify each factor's contribution to the total changes in TCF for each domain in Fig. 1C. The results reveal that the change in TC genesis (dg) was the primary contributor to the total change in TCF for all domains (Fig. 2A). The changes in TC genesis frequency of occurrence (i.e., TGF; "Observed data" section) for δALL21 (Fig. 1E) reveal similar changes to those for TCF (Fig. 1C).

Impact of anthropogenic aerosols on global TC genesis

To further elucidate what caused the TGF changes in the domains indicated by the blue boxes in Fig. 1E, we applied a recently developed (*13*) dynamic TC genesis potential index (DGPI) ("GPI and variational method" section). The DGPI consists of four dynamical factors, and the DGPI changes adequately reflect the TGF changes (Fig. 2B). By applying a variational method ("GPI and variational method" section), we were able to identify which element of the DGPI is responsible for the total changes in DGPI (Fig. 2, C to F). It turns out that the changes in upward midlevel motion (ω$_{500}$) is the
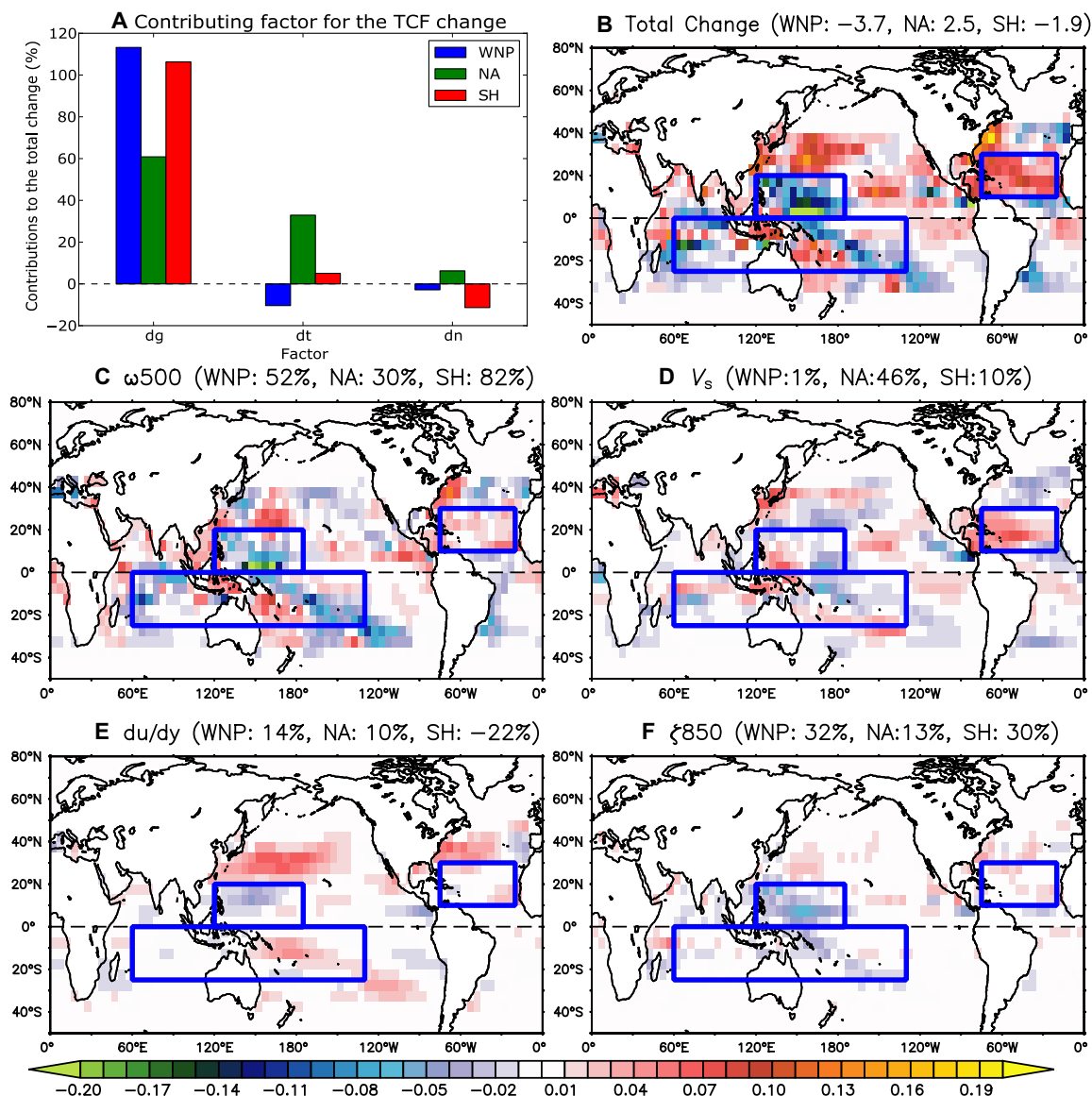
Fig. 2. Empirical and DGPI analysis to identify the causes for the TCF and TGF changes. (**A**) Fractional contribution of each term to the TCF changes. TCF changes over the three tropical domains (black rectangles in Fig. 1A) are decomposed into TC genesis change (dg), TC track change (dt), and other nonlinear effects (dn) through an empirical statistical analysis. (**B** to **F**) Fractional contribution of each term to the total DGPI change. The total DGPI changes (B) are decomposed into each term's contribution through a variational method by (C) ω_{500} (vertical velocity at 500 hPa), (D) V_s (vertical wind shear between 200 hPa and 500 hPa), (E) du/dy (meridional shear vorticity at 500 hPa), and (F) ζ_{850} (absolute vorticity at 850 hPa). The numbers in (B) denote the area mean changes in DGPI over the three tropical domains, while the numbers in (C) to (F) denote the fractional contributions to the total changes for each domain and each variable.

primary contributor to the decreases in DGPI in the WNP and SH, whereas the changes in vertical wind shear is the primary contributor to the increase in DGPI in the NA. These results suggest substantial changes in large-scale circulations caused by the changes in anthropogenic aerosols, which, in turn, have led to the changes in TGF.

To help us interpret what is indicated by the results of the DGPI analysis, Fig. 3 (A and B) shows the mean circulation at the 200-hPa level simulated in the CNTL experiment. The three domains of interest are actually located between the subtropical westerly jets in both hemispheres, and the simulated mean wind speed at 200 hPa is relatively weaker (Fig. 3A). The WNP and SH domains are also located near the center of divergence fields in the upper troposphere,

whereas the NA domain is located where the convergence fields are in the upper troposphere climatologically (Fig. 3B). The changes in upper-tropospheric winds simulated by ALL21 show alternating patterns, revealing poleward shifts of the subtropical westerly jets (Fig. 3C). The tropical NA is subject to weakened westerly winds (Fig. 1C), which, in turn, lead to reduced vertical wind shear, resulting in increased TC activity. In contrast, the mean changes in the divergent winds show convergence anomalies over the WNP and SH domains (Fig. 3D), revealing that the mean upward motion was weakened over these domains, which, in turn, led to decreased TGF and TCF. Overall, these changes are consistent with the DGPI analysis and could be the primary reason for the changes in TC activity.
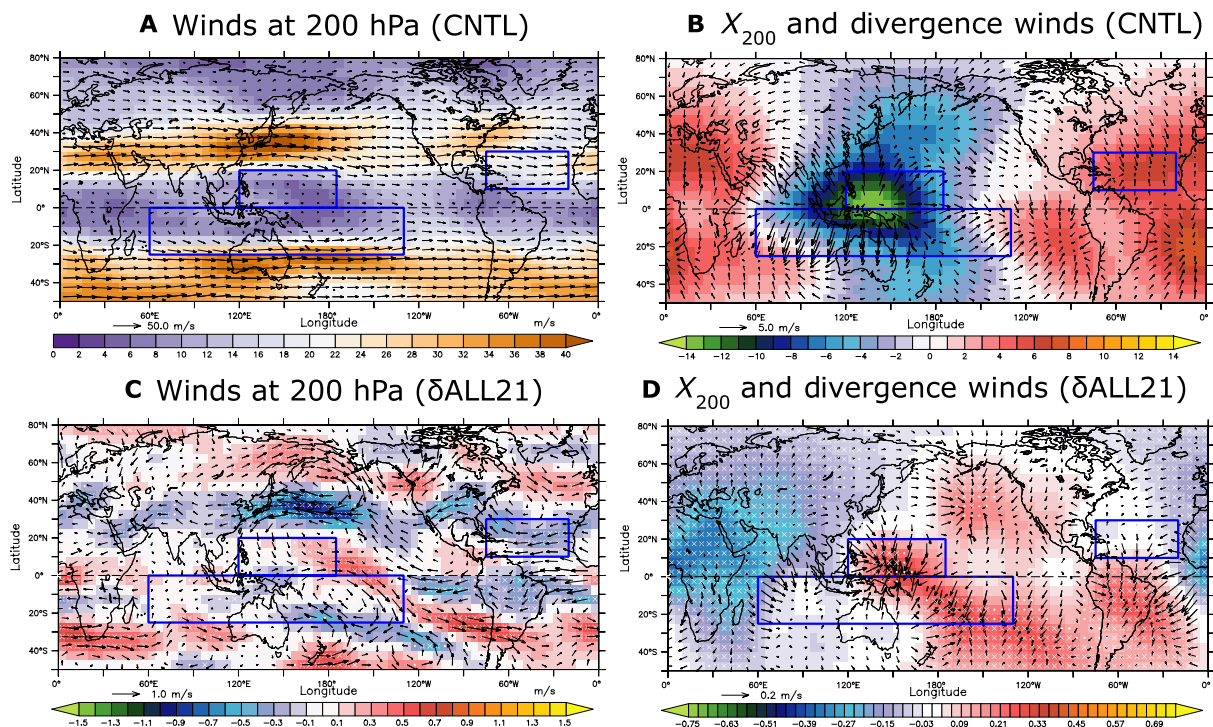
Fig. 3. Simulated mean large-scale circulation and the changes in the upper troposphere. (**A**) The mean winds at 200 hPa (vectors) and the wind speed for the zonal component (shading) simulated by the CNTL experiment. (**B**) The mean velocity potential (shading) and divergent winds (vectors) at 200 hPa simulated by the CNTL experiment. (**C** and **D**) As in (A) and (B) but for the simulated differences between the ALL21 and CNTL experiments. White crosses (dots) indicate where the difference in zonal wind over the grid cell is statistically significant at the 95% (90%) level according to the bootstrap method. Units: m s^{-1} for wind speed and divergent winds; 10^6 m^2 s^{-1} for velocity potential.

Impact of regional aerosol changes on TCs globally

As indicated in Fig. 1F, the decadal changes in anthropogenic sulfate aerosols since 1980 are not spatially homogeneous: They decrease over Europe and the United States but increase over South and East Asia. Therefore, these different signs of change may exert different changes in global TC activity. To investigate this hypothesis, we conducted two further climate model simulations like ALL21 but with separately prescribed decreased emissions of anthropogenic aerosols over Europe and the United States (W21; Fig. 4A) and increased emissions of aerosols over South and East Asia (IP21; Fig. 4E and Table 1). Figure 4 (B and F) reveals the changes in TCF simulated by the W21 and IP21 runs relative to the CNTL experiment, respectively. The simulated changes in TCF reveal somewhat similar changes between δW21 and δIP21; however, there are some substantial differences in the detail. For example, the increases in TCF in the NA are significant in δW21 but not in δIP21 (Fig. 4, B and F, and Table 2). On the other hand, both δW21 and δIP21 reveal decreased TCF in the WNP but more significantly in δIP21 than in δW21. The decreased TCF in the SH is significant in δW21 but not in δIP21. The changes in large-scale circulations also reflect these TCF differences (Fig. 4, C, D, G, and H). Although both δW21 and δIP21 show a poleward shift in the subtropical westerly jets in the Northern Hemisphere (NH), the shift is further extended to the NA in δW21 but is not extended in δIP21 (Fig. 4, C and G). Therefore, the increases in TCF in the NA in δALL21 are more attributable to the decreased anthropogenic aerosols in Europe and the United States, whereas the effect of increased aerosols in South and East

Asia imposes minimal effects on the TCF and TGF changes in the NA. Meanwhile, the decreases in TCF and TGF in the SH simulated by δALL21 are more attributable to the decreased anthropogenic aerosols in Europe and the United States via the increasing convergence in the upper troposphere over the SH (Table 2 and Fig. 4D).

DISCUSSION

We speculate that the reduction in anthropogenic aerosols in Europe and the United States has caused hemispheric heating in the NH relative to the SH, which, in turn, has led to anomalous meridional atmospheric overturning circulation. More specifically, the NH acts as an ascending branch, whereas the SH acts as a descending branch, meaning convective activity is suppressed in the SH, leading to fewer TCs being generated there. As for the WNP, the effect of increased anthropogenic aerosols from India and China might have played a major role in the decreased TCF and TGF in the WNP relative to the decreased aerosols in Europe and the United States. The increases in anthropogenic aerosols might have led to a cooling over the Asian continent, thereby reducing the thermal contrast between the Asian continent and the Indo-Pacific oceans, in turn leading to a weakening of the Asian monsoon circulation in the boreal summer (Fig. 5). Accordingly, the monsoon trough, which is one of the major sources of TC genesis in the WNP (*14*), would be weakened in the summer, resulting in decreased TCF and TGF over the WNP (Fig. 5).
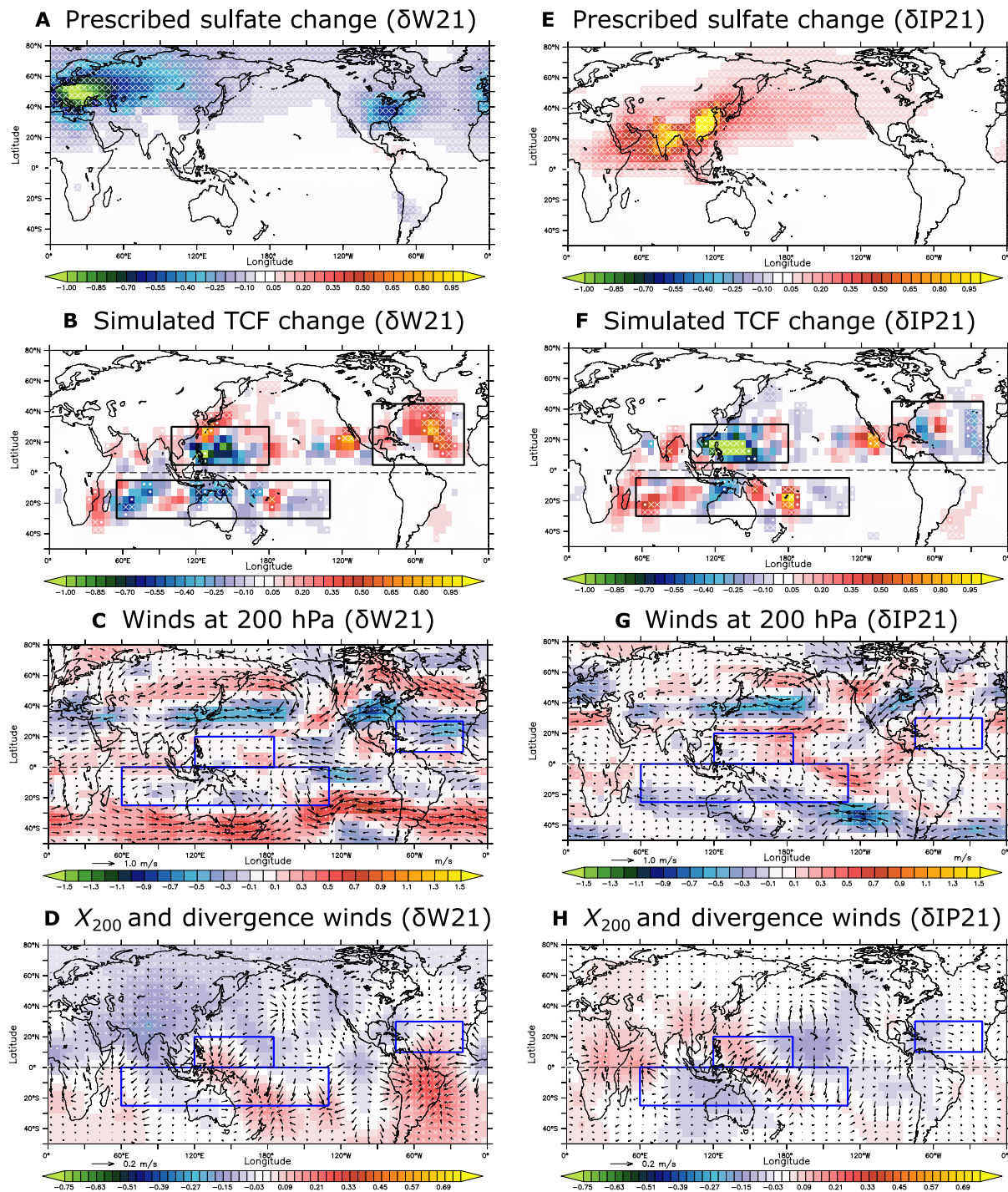
Fig. 4. Simulated changes by the additional idealized aerosol-prescribed experiments. (**A** to **D**) Idealized experiments prescribed with decreased emissions of anthropogenic aerosols over Europe and the United States only (W21). (**E** to **H**) As in (A) to (D) except for increased emissions of anthropogenic aerosols over South and East Asia (IP21). (A) and (E), (B) and (F), (C) and (G), and (D) and (H) are the same as in Figs. 1 (F and C) and 3 (C and D) but for W21 and IP21, respectively.

The weakening of vertical wind shear in NA could be partially the result of local ocean warming by the decreased anthropogenic aerosols through the wind-evaporation-SST feedback (15–16) as an analogy of Atlantic Meridional Mode (AMM) (17–19). The surface ocean warming might have caused a northward shift of the Inter-tropical Convergence Zone that, in turn, leads to a northward shift

in ascending branch of the Hadley circulation that reduces upper-level westerlies around the main development region of Atlantic TCs. Meanwhile, it is argued that AMM is an intrinsic atmosphere-ocean coupled internal mode, and its decadal variation might have caused decadal variations in hydroclimate including TCs in the NA over the past 40 years (16, 19). Because the SPEAR (Seamless System for

Table 1. Experimental settings. Listed are the experiment names, prescribed emissions of anthropogenic aerosols, prescribed level for other external forcings (e.g., greenhouse gases and ozone), and the number of simulation years.

Name	Prescribed anthropogenic aerosols	Other external forcing	Simulation years
CNTL	1980–2000 mean		
ALL21	2001–2020 mean		
W21	As in CNTL except for the 2001–2020 mean over Europe and US	Fixed level at 2000	200
IP21	As in CNTL except for the 2001–2020 mean over South and East Asia		

Table 2. Observed and simulated changes in TCF and TGF. Observed and simulated changes were computed over the tropical domains of the WNP, NA, and SH for TCF (black rectangles in Fig. 1A) and TGF (blue rectangles in Fig. 1E). The bold numbers indicate where the change is statistically significant at the 95% level based on a bootstrap method. Numbers in parentheses denote the P value.

	TCF			
	Period or difference	Fractional difference (P value)		
		WNP	NA	SH
Observations	2001–2020 minus 1980–2000	**−22.3%** (0.03)	**30.6%** (0.01)	**−34.5%** (0.00)
δALL21	ALL21 minus CNTL	**−4.8%** (0.01)	**8.7%** (0.00)	**−6.4%** (0.01)
δW21	W21 minus CNTL	−1.4% (0.46)	**6.5%** (0.03)	**−4.8%** (0.03)
δIP21	IP21 minus CNTL	**−4.1%** (0.04)	−1.8% (0.60)	1.9% (0.36)

	TGF			
	Period or difference	Fractional difference (P value)		
		WNP	NA	SH
Observations	2001–2020 minus 1980–2000	**−13.8%** (0.02)	**33.6%** (0.00)	**−15.9%** (0.01)
δALL21	ALL21 minus CNTL	**−5.9%** (0.00)	**8.1%** (0.01)	**−7.0%** (0.00)
δW21	W21 minus CNTL	−2.8% (0.11)	4.7% (0.13)	**−3.9%** (0.03)
δIP21	IP21 minus CNTL	**−4.6%** (0.01)	−2.0% (0.55)	2.4% (0.19)

Prediction and Earth System Research) model reasonably simulates AMM in terms of the amplitude and power spectrum as observed (fig. S1), we estimated how much the decadal variation in AMM can potentially affect the TCF increases relative to the effect of anthropogenic aerosol forcing (Fig. 6). Overall, the SPEAR experiments reveal that the decadal variation in AMM might have partially contributed to the increasing TCF over the NA, but the increases in TCF are not as large as the increases through the effect of anthropogenic aerosols.

In this study, we applied a newly developed DGPI to the analysis of TGF changes. This is because the simulated changes in DGPI were relatively more consistent with the simulated changes in TGF than those in the other conventional GPI formula. For example, another GPI commonly used is Emanuel and Nolan's GPI (20). Although this GPI also reproduced a similar spatial pattern in the changes to the changes in TGF and DGPI for δALL21, this GPI is markedly inconsistent with the total changes in TGF over the key domains of the tropical WNP and the SH (fig. S2). Most of the GPI formula had been optimized on the basis of the observed TGF and reanalysis data for the present-day climate but not on the basis of the different climates such as future projections. Therefore, particular attention should be directed to the uncertainty in the usage of GPIs for interpreting the changes in TGF in different climates.

As reviewed earlier, previous studies have reported the effects of anthropogenic aerosols on TC activity at local scales from a thermodynamical point of view. For example, aerosol loading over the open oceans can inhibit solar insolation at the surface, leading to cooler surface oceans that, in turn, lead to suppressed convection and decreased TC activity (7). This paper adds one more important aspect to the dynamical viewpoint. The decreased anthropogenic aerosols in Europe and the United States must have caused anomalous heating in the mid-latitudes of the NH, thereby causing reduced meridional gradients of atmospheric temperature. This, in turn, will have led to a poleward shift in the subtropical jets, thereby altering the vertical wind shear that is important for TC activity in the NA. The additional heating in the mid-latitudes in the NH might have also induced subsidence anomalies over the tropics in the SH, thereby reducing the frequency of TCs over the SH.

Note that although the signs of the changes in TCF and TGF in δALL21 are consistent with the observed changes over the past 40 years in most regions, quantitatively the changes are different from each other (Table 2). This is because other factors aside from

anthropogenic aerosols might also have been involved in the observed changes in global TC activity since 1980. As reported in one of our previous studies (5), greenhouse gases, volcanic eruptions, and multidecadal natural variability might also have played important roles in the observed changes in TCs globally since 1980. Also, a rigorous estimate of quantitative contribution of anthropogenic aerosols to the observed changes in TCF remains challenging in this study. This is because the idealized experiments that we applied were so-called fixed forcing experiments in which long-term simulations were conducted with the fixed level of anthropogenic forcing. This allows modeled climate system to adjust more than it would via a transient response to forcing changes occurring over a 40-year period.

Another caveat is that the SPEAR model systematically underestimates intense TCs such as the Saffir-Simpson category 3–5 TCs (maximum wind speed ≥ 50 m s^{-1}) because the 50-km mesh horizontal resolution is not high enough to resolve the intense TCs. Because the observed changes in TCF for category 3–5 TCs are somewhat different from those for all storms including both weaker and intense TCs (Fig. 7), there might be uncertainty in the model results for which category 3–5 TCs are missing. However, we may be able to investigate whether the simulated changes of TCF in the relatively intense TCs for the SPEAR model are consistent with these in the observed category 3–5 TCs. It turned out that the threshold of 50 m s^{-1} for the observed category 3–5 TCs corresponds
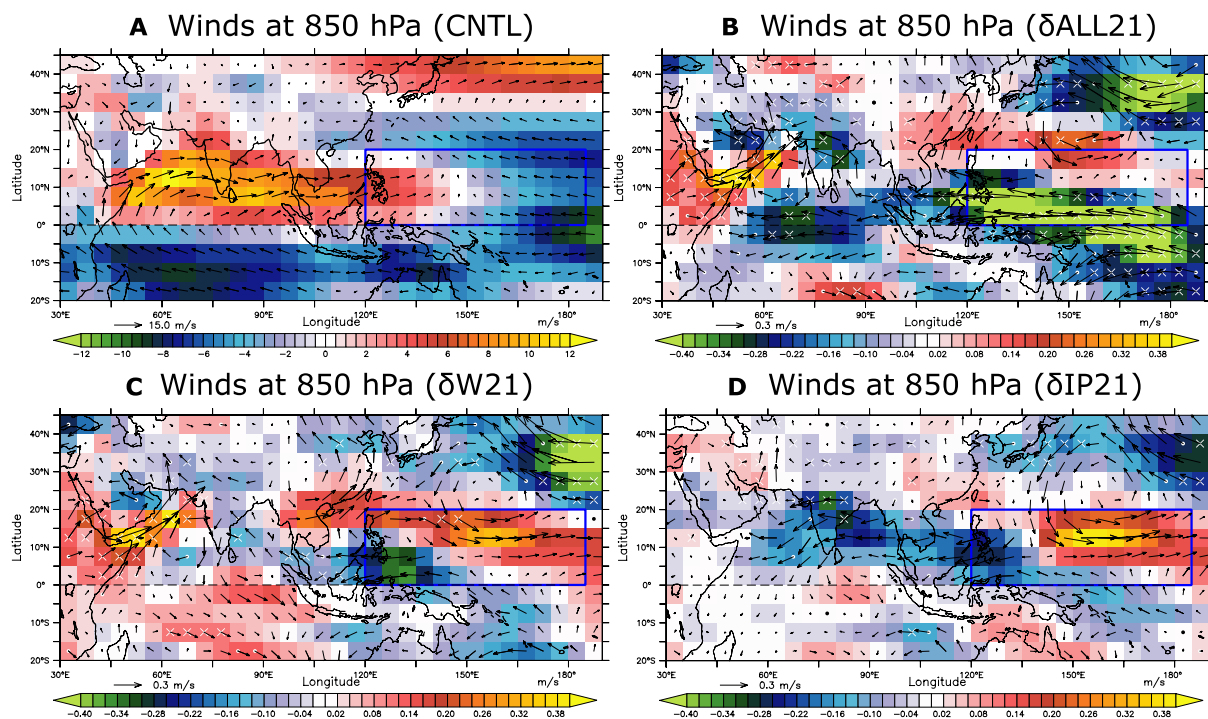
Fig. 5. Simulated Asian monsoon and its changes. (**A**) Mean winds at 850 hPa (vectors) and the wind speed for the zonal component (shading) during July–October simulated by the CNTL experiment. (**B**) As in (A) but for the simulated differences between the ALL21 and CNTL experiments. (**C** and **D**) As in (B) but for the W21 and IP21 experiments, respectively. White crosses (dots) indicate where the difference in zonal wind over the grid cell is statistically significant at the 95% (90%) level according to the bootstrap method. Units: m s^{-1}.
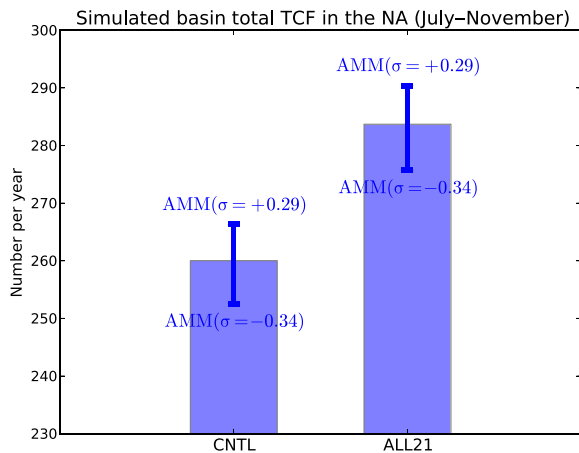
Fig. 6. Simulation basin total July–November TCF over the North Atlantic Ocean. (**A**) The histogram shows the July–November mean basin total TCF over the North Atlantic during July–November through the 200-year simulations (CNTL and ALL21) by SPEAR. The error bars show the regressed range of July–November basin total TCF between AMM index +0.29σ and −0.34σ in the SPEAR simulations. The simulated basin total TCF was linearly regressed onto the simulated AMM index. Then, the TCF values at the specific AMM index values were computed using the linear relationship. Given the fact that the observed July–November averaged AMM index was +0.29σ over the period 2001–2020 and −0.34σ over the period 1980–2000, the range of computed regressed TCF values between AMM index +0.29σ and −0.34σ is assumed to be the effect of decadal change in AMM on TCF variation in the SPEAR model. This figure highlights that AMM affects the basin total TCFs in the model, but the magnitude of the AMM effect, as measured by the length of error bars, is not as large as the mean difference caused by anthropogenic aerosols (i.e., mean difference between ALL21 and CNTL).

to the 87th percentile for the intensity of all storms in observations. The same 87th percentile of the storm intensity for all simulated TCs by the SPEAR model corresponds to 37 m s^{-1}. Therefore, the simulated storms with a maximum wind speed of 37 m s^{-1} or greater may be considered as "category 3–5 equivalent TCs" to represent intense TCs in the SPEAR model. The SPEAR model through δALL21 shows a similar spatial pattern of the TCF changes in the category 3–5 equivalent TCs to that of the observed category 3–5 TCs (Fig. 7). This indicates that, consistent with observations, the SPEAR model shows the different responses of TCF between weaker and intense storms to the aerosol forcing. Meanwhile, it would be preferable to use a high-resolution model that can simulate intense TCs to minimize uncertainty.
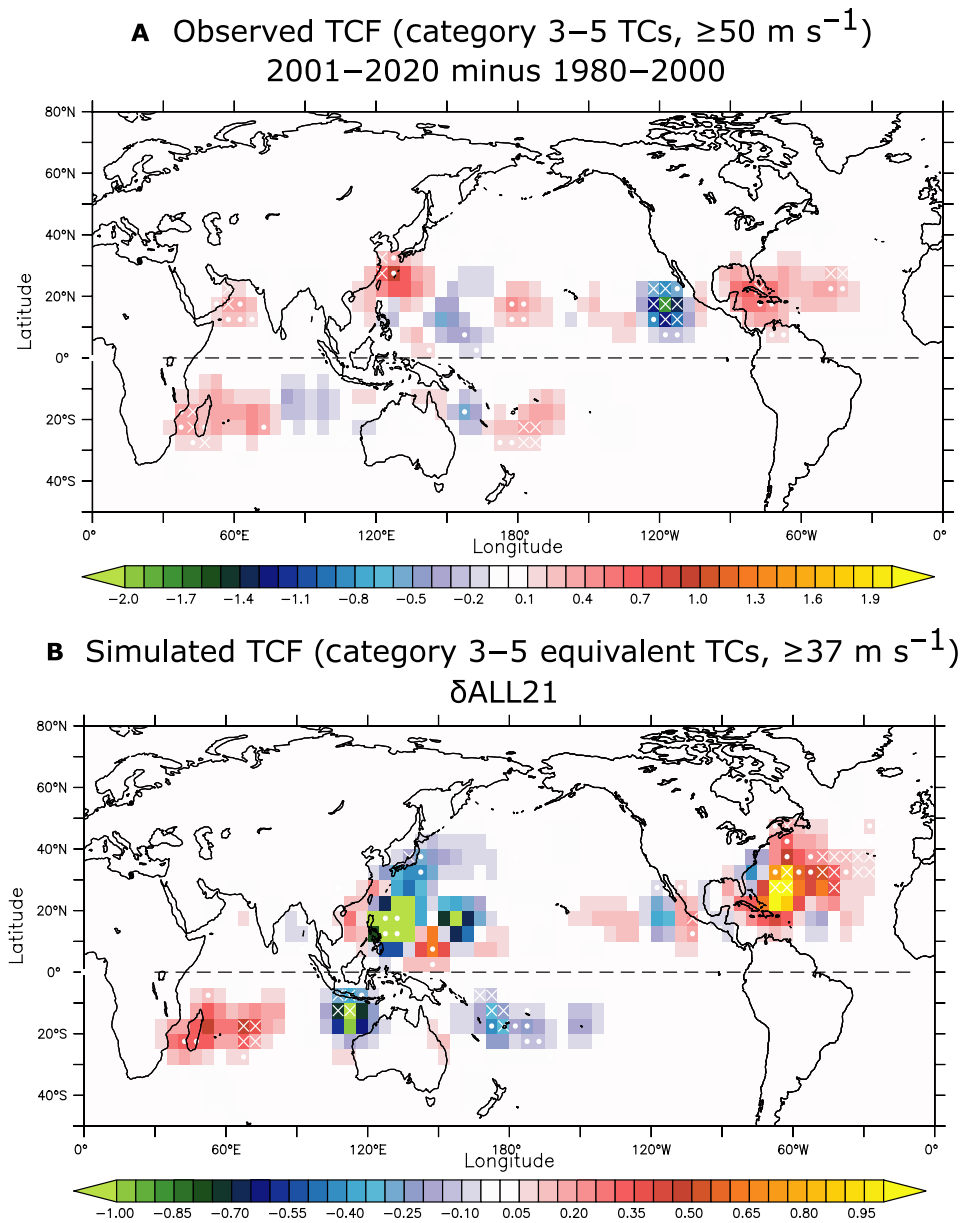
Last, it is important to emphasize that changes in anthropogenic aerosols, as well as greenhouse gases, apparently can exert substantial impacts on global TC activity, which delivers an important message to society regarding the seriousness of the impacts our activities are having and therefore the political decisions we make in the future in terms of changes in emissions and their potential impacts on TC activity on the global scale.

MATERIALS AND METHODS
Observed data
The International Best Track Archive for Climate Stewardship (*21*), version 4, was used over the period 1980–2020 for the TC data. We defined a TC by the lifetime maximum intensity being greater than or equal to 34 knots (i.e., 17.5 m s^{-1}) in the observations. As in our previous study (*5*), only TC positions with maximum surface wind speeds of 34 knots or greater were counted every 6 hours over each

A Observed TCF (category 3–5 TCs, ≥50 m s^{-1})
2001–2020 minus 1980–2000

B Simulated TCF (category 3–5 equivalent TCs, ≥37 m s^{-1})
δALL21

Fig. 7. Observed and simulated changes in category 3–5 TCs. (A) Mean difference in the observed TCF for the storm locations with maximum surface wind speeds of 50 m s^{-1} or greater. **(B)** As in (A) but for the simulated difference between ALL21 and CNTL in terms of the category 3–5 equivalent TCs (≥37 m s^{-1}). It turned out that the threshold of 50 m s^{-1} for the observed category 3–5 TCs corresponds to the 87th percentile for the intensity of all storms in the observations. The same 87th percentile in the SPEAR model corresponds to 37 m s^{-1}. Therefore, the simulated storms with a maximum wind speed of 37 m s^{-1} or greater are considered as category 3–5 equivalent TCs in the SPEAR model.

5° × 5° grid box globally. The total count for each grid box was defined as the TCF. The TCF fields were further smoothed using a nine-point moving average weighted by distance from the center of the grid box. The same computation was also applied to TC genesis (i.e., the TGF). The monthly mean large-scale parameters, such as 200- and 850-hPa winds, were derived from the Japanese 55-year Reanalysis (22) over the same period of 1980–2020.

Model
The Geophysical Fluid Dynamics Laboratory Seamless System for Prediction and Earth System Research (SPEAR) (23) was used for

the climate model simulations. SPEAR consists of the new AM4-LM4 atmosphere and land surface model (24, 25), the MOM6 ocean model (https://github.com/NOAA-GFDL/MOM6), and the SIS2 sea-ice model (26). The horizontal resolution of the ocean and ice components is 1° × 1° while that of the atmosphere and land surface is an approximate 50-km mesh. Note that SPEAR simulates the mass distribution of five aerosol types: sulfates, dust, black carbon, organic carbon, and sea salt. The concentrations in the model are calculated on the basis of the emissions, chemical production for sulfate and secondary organics, dry and wet deposition, transport by advection, and dry and wet convection (24). Specifically, SPEAR

includes a physical process that interacts between aerosols and convection (i.e., the aerosol indirect effect) (*24*).

Model-simulated TCs were obtained directly from 6-hourly outputs using the scheme documented by Harris *et al.* (*27*). In short, the flood fill algorithm is applied to find closed contours of sea level pressure anomalies along with 1-K temperature anomalies to identify the warm core. The storm detection must maintain above certain conditions, as well as a specified relaxed wind speed criterion (i.e., 15.75 m s^{-1}) due to the 50-km horizontal resolution, for at least 36 consecutive hours.

Model experiments

We conducted four types of climate simulations using SPEAR by prescribing various spatial patterns of emissions of anthropogenic aerosols. A summary of the experiments is provided in Table 1. These experiments are so-called long-term climate simulations prescribed with fixed anthropogenic forcing. The simulations were initiated from the random restart files derived from the 1000-year preindustrial control experiments. The simulation length was 210 years, but the first 10 years were disregarded as the spin-up period. In the experiments, the solar constant and all anthropogenic forcings except that of anthropogenic aerosols (e.g., greenhouse gases and ozone) were fixed at the year 2000 level. The only differences among the four experiments were the prescribed emissions of anthropogenic aerosols (i.e., sulfur dioxide, sulfates, black carbon, and organic carbon emissions caused by human activity including agriculture, industrial, transportation, residential, commercial, solvent production, and waste). In the model, in addition to the above anthropogenic aerosol emissions, dust emissions are calculated interactively using a threshold for wind erosion, and sea salt emissions are also computed interactively. The CNTL experiment was prescribed with the mean emissions of anthropogenic aerosols over the period 1980–2000, and a counter experiment (ALL21) was prescribed with the mean emissions of anthropogenic aerosols over the period 2001–2020. Therefore, the difference between ALL21 and CNTL (i.e., δALL21) represented the difference in the emissions of anthropogenic aerosols between 1980–2000 and 2001–2020. An idealized experiment, W21, was also conducted, which was identical to ALL21 except that only the changes in emissions of anthropogenic aerosols over Europe and the United States were included, with the rest of the world remaining unchanged from CNTL. Another idealized experiment, IP21, was also carried out. This was again identical to ALL21 except that only the changes in emissions of aerosols over South and East Asia were included.

Empirical statistical analysis for TCs

To reveal the relative importance of TC genesis, TC tracks, and their combinations for the changes in local TCF, we applied the empirical statistical analysis technique developed by Yokoi and Takayabu (*11*) and Murakami *et al.* (*12*). Full details of the method are of course available in those references; however, in short, the climatological mean TCF in a 5° × 5° grid cell can be written as follows

$$\overline{f(A)} = \iint_C \overline{g(A_0)} \times \overline{t(A, A_0)} \, dA_0 \tag{1}$$

where $f(A)$ is the TCF in a specific grid cell A, the overline indicates a climatological mean, $g(A_0)$ is the frequency of TC genesis in grid cell A_0, $t(A, A_0)$ is the probability that a TC generated in grid cell A_0

propagates to grid cell A, and C is the entire global domain over which the integration is performed. The change in TCF over grid A simulated by an idealized experiment relative to the reference experiment can be written as follows

$$\delta f(A) = \underbrace{\iint_C \delta g(A_0) \times \overline{t(A, A_0)} \, dA_0}_{dg} + \underbrace{\iint_C \overline{g(A_0)} \times \delta t(A, A_0) \, dA_0}_{dt} + \underbrace{\iint_C \delta g(A_0) \times \delta t(A, A_0) \, dA_0}_{dn} \tag{2}$$

where δ is the simulated change of an experiment relative to the reference experiment (e.g., δALL21). The simulated change in TCF can be decomposed into three factors: (i) TC genesis distribution change (first term, dg); (ii) TC track change (second term, dt); and (iii) the nonlinear effect (third term, dn). After computing these three terms for each grid, the area averages of these are computed for the domains of interests (blue rectangles in Fig. 1E) to reveal the factors responsible for the changes in local TCF over the domains (Fig. 2A).

GPI and variational method

A new GPI developed by Wang and Murakami (*13*) was applied to the climate simulations to quantify the large-scale parameters responsible for the changes in TGF. Unlike the conventional GPI formula, the new GPI, termed the dynamical GPI (DGPI), consists of four dynamical parameters only, as follows

$$DGPI = (2.0 + 0.1 \times V_s)^{-1.7} \left(5.5 - \frac{du_{500}}{dy} \times 10^5\right)^{2.3}$$
$$(5.0 - 20 \times \omega_{500})^{3.4} (5.5 + |\zeta_{a500} \times 10^5|)^{2.4} e^{-11.8} - 1.0 \tag{3}$$

where V_s represents the vertical wind shear, which is defined as the magnitude of the difference in wind speed between the 200- and 850-hPa levels (units: m s^{-1}); ζ_{a850} is the absolute vorticity at the 850-hPa level (s^{-1}); ω_{500} represents the vertical p velocity (Pa s^{-1}) at 500 hPa; and du_{500}/dy denotes the meridional shear vorticity associated with the zonal wind at 500 hPa (u_{500}, s^{-1}). Wang and Murakami (*13*) revealed a reasonable representation of the climatological mean of global TGF in addition to the interannual variations relative to observations. Note that the DGPI is not completely independent of the thermodynamic factors. DGPI implicitly includes the thermodynamic effect by incorporating the vertical motion term (ω_{500}). ω_{500} is highly correlated with midlevel relative humidity. In general, mean upward motion is important for TC genesis because the boundary layer flows converge and the upward transfer of moisture increases the midlevel relative humidity (*13*). Both the dynamic and thermodynamic conditions are also conducive to the initiation of organized convection or incipient cyclonic circulation (i.e., the "seeds"). DGPI is also significantly correlated with SST and maximum potential intensity (*13*).

To quantify which of the changes in the four variables in the DGPI were responsible for the changes in the DGPI between the two climate simulations, we applied a variational method. The changes in DGPI can be decomposed into four factors, as follows

$$\Delta DGPI = \Delta F1 \cdot \overline{F2 \cdot F3 \cdot F4} + \Delta F2 \cdot \overline{F1 \cdot F3 \cdot F4} + \Delta F3 \cdot \overline{F1 \cdot F2 \cdot F4} + \Delta F4 \cdot \overline{F1 \cdot F2 \cdot F3} \tag{4}$$

where the overbar represents the mean of a reference experiment (i.e., CNTL) and Δ represents the change of an experiment relative to the reference experiment. *F* represents each component term of the DGPI. Each term of Eq. 4 represents the fractional contribution to the total DGPI change. The total changes (left-hand side of Eq. 4) are shown in Fig. 2A, and each term's contributions are shown in Fig. 2 (C to F). The fractional changes relative to the total change are computed for each term and domain of interest (blue rectangles in Fig. 2, C to F), and the domain mean fractional changes are denoted by the numbers in each panel in Fig. 2 (C to F).

SUPPLEMENTARY MATERIALS
Supplementary material for this article is available at https://science.org/doi/10.1126/sciadv.abn9493

REFERENCES AND NOTES

1. T. Knutson, S. J. Camargo, J. C. L. Chan, K. Emanuel, C.-H. Ho, J. Kossin, M. Mohapatra, M. Satoh, M. Sugi, K. Walsh, L. Wu, Tropical cyclones and climate change assessment: Part I. Detection and attribution. *Bull. Am. Meteorol. Soc.* **100**, 1987–2007 (2019).

2. T. Knutson, S. J. Camargo, J. C. L. Chan, K. Emanuel, C.-H. Ho, J. Kossin, M. Mohapatra, M. Satoh, M. Sugi, K. Walsh, L. Wu, Tropical cyclones and climate change assessment: Part II. Projected response to anthropogenic warming. *Bull. Am. Meteorol. Soc.* **101**, E303–E322 (2020).

3. J. P. Kossin, K. A. Emanuel, G. A. Vecchi, The poleward migration of the location of tropical cyclone maximum intensity. *Nature* **509**, 349–352 (2014).

4. J. P. Kossin, A global slowdown of tropical cyclone translation speed. *Nature* **558**, 104–107 (2018).

5. H. Murakami, T. L. Delworth, W. F. Cooke, M. Zhao, B. Xiang, P.-C. Hsu, Detected climatic change in global distribution of tropical cyclones. *Proc. Natl. Acad. Sci. U.S.A.* **117**, 10706–10714 (2020).

6. S. Wang, R. Toumi, Recent migration of tropical cyclones toward coasts. *Science* **371**, 514–517 (2021).

7. N. J. Dunstone, D. M. Smith, B. B. B. Booth, L. Hermanson, R. Eade, Anthropogenic aerosol forcing of Atlantic tropical storms. *Nat. Geosci.* **6**, 534–539 (2013).

8. A. T. Evan, J. P. Kossin, C. Chung, V. Ramanathan, Arabian Sea tropical cyclones intensified by emissions of black carbon and other aerosols. *Nature* **479**, 94–97 (2011).

9. B. Wang, J. Liu, H.-J. Kim, P. J. Webster, S.-Y. Yim, B. Xiang, Northern Hemisphere summer monsoon intensified by mega-El Niño/southern oscillation and Atlantic multidecadal oscillation. *Proc. Natl. Acad. Sci. U.S.A.* **110**, 5347–5352 (2013).

10. C. K. Folland, D. E. Parker, A. Colman, R. Washington, Large scale modes of ocean surface temperature since the late nineteenth century, in *Beyond El Niño: Decadal and Interdecadal Climate Variability*, A. Navarra, Ed. (Springer-Verlag, 1999), pp. 73–102.

11. S. Yokoi, Y. N. Takayabu, Attribution of decadal variability in tropical cyclone passage frequency over the Western North Pacific: A new approach emphasizing the genesis location of cyclones. *J. Climate* **26**, 973–987 (2013).

12. H. Murakami, B. Wang, T. Li, A. Kitoh, Projected increase in tropical cyclones near Hawaii. *Nat. Clim. Chang.* **3**, 749–754 (2013).

13. B. Wang, H. Murakami, Dynamic genesis potential index for diagnosing present-day and future global tropical cyclone genesis. *Environ. Res. Lett.* **15**, 114008 (2020).

14. E. A. Ritchie, G. J. Holland, Large-scale patterns associated with tropical cyclogenesis in the western Pacific. *Mon. Weather Rev.* **127**, 2027–2043 (1999).

15. S.-P. Xie, A dynamic ocean-atmosphere model of the tropical Atlantic decadal variability. *J. Climate* **12**, 64–70 (1999).

16. P. Chang, L. Ji, H. Li, A decadal climate variation in the tropical Atlantic Ocean from thermodynamic air-sea interactions. *Nature* **385**, 516–518 (1997).

17. J. C. H. Chiang, D. J. Vimont, Analogous Pacific and Atlantic meridional modes of tropical atmosphere-ocean variability. *J. Climate* **17**, 4143–4158 (2004).

18. D. J. Vimont, J. P. Kossin, The Atlantic meridional mode and hurricane activity. *Geophys. Res. Lett.* **34**, L07709 (2007).

19. J. P. Kossin, D. J. Vimont, A more general framework for understanding Atlantic hurricane variability and trends. *Bull. Am. Meteorol. Soc.* **88**, 1767–1782 (2007).

20. K. A. Emanuel, D. S. Nolan, Tropical cyclone activity and global climate. Preprints, in *Proceedings of the 26th Conference on Hurricanes and Tropical Meteorology* (2004), Miami, FL, American Meteorological Society, pp. 240–241.

21. K. R. Knapp, M. C. Kruk, D. H. Levinson, H. J. Diamond, C. J. Neuman, The international best track archive for climate stewardship (IBTrACS). *Bull. Am. Meteor. Soc.* **91**, 363–376 (2010).

22. S. Kobayashi, Y. Ota, Y. Harada, A. Ebita, M. Moriya, H. Onoda, K. Onogi, H. Kamahori, C. Kobayashi, H. Endo, K. Miyaoka, K. Takahashi, The JRA-55 reanalysis: General specifications and basic characteristics. *J. Meteorol. Soc. Japan* **93**, 5–48 (2015).

23. T. L. Delworth, W. F. Cooke, A. Adcroft, M. Bushuk, J.-H. Chen, K. A. Dunne, P. Ginoux, R. Gudgel, R. W. Hallberg, L. Harris, M. J. Harrison, N. Johnson, S. B. Kapnick, S.-J. Lin, F. Lu, S. Malyshev, P. C. Milly, H. Murakami, V. Naik, S. Pascale, D. Paynter, A. Rosati, M. D. Schwarzkopf, E. Shevliakova, S. Underwood, A. T. Wittenberg, B. Xiang, X. Yang, F. Zeng, H. Zhang, L. Zhang, M. Zhao, SPEAR: The next generation GFDL modeling system for seasonal to multidecadal prediction and projection. *J. Adv. Model. Earth Syst.* **12**, e2019MS001895 (2020).

24. M. Zhao, J.-C. Golaz, I. M. Held, H. Guo, V. Balaji, R. Benson, J.-H. Chen, X. Chen, L. J. Donner, J. P. Dunne, K. A. Dunne, J. Durachta, S.-M. Fan, S. M. Freidenreich, S. T. Garner, P. Ginoux, L. M. Harris, L. W. Horowitz, J. P. Krasting, A. R. Langenhorst, Z. Liang, P. Lin, S.-J. Lin, S. L. Malyshev, E. Mason, P. C. D. Milly, Y. Ming, V. Naik, F. Paulot, D. Paynter, P. Phillipps, A. Radhakrishnan, V. Ramaswamy, T. Robinson, D. Schwarzkopf, C. J. Seman, E. Shevliakova, Z. Shen, H. Shin, L. Silvers, J. R. Wilson, M. Winton, A. T. Wittenberg, B. Wyman, B. Xiang, The GFDL global atmospheric and land model AM4.0/LM4.0 – Part I: Simulation characteristics with prescribed SSTs. *J. Adv. Model. Earth Syst.* **10**, 735–769 (2018).

25. M. Zhao, J.-C. Golaz, I. M. Held, H. Guo, V. Balaji, R. Benson, J.-H. Chen, X. Chen, L. J. Donner, J. P. Dunne, K. A. Dunne, J. Durachta, S.-M. Fan, S. M. Freidenreich, S. T. Garner, P. Ginoux, L. M. Harris, L. W. Horowitz, J. P. Krasting, A. R. Langenhorst, Z. Liang, P. Lin, S.-J. Lin, S. Malyshev, E. Mason, P. C. D. Milly, Y. Ming, V. Naik, F. Paulot, D. Paynter, P. Phillipps, A. Radhakrishnan, V. Ramaswamy, T. Robinson, D. Schwarzkopf, C. J. Seman, E. Shevliakova, Z. Shen, H. Shin, L. Silvers, J. R. Wilson, M. Winton, A. T. Wittenberg, B. Wyman, B. Xiang, The GFDL global atmospheric and land model AM4.0/LM4.0 – Part II: Model description, sensitivity studies, and turning strategies. *J. Adv. Model. Earth Syst.* **10**, 735–769 (2018).

26. A. Adcroft, W. Anderson, V. Balaji, C. Blanton, M. Bushuk, C. O. Dufour, J. P. Dunne, S. M. Griffies, R. Hallberg, M. J. Harrison, I. M. Held, M. F. Jansen, J. G. John, J. P. Krasting, A. R. Langenhorst, S. Legg, Z. Liang, C. M. Hugh, A. Radhakrishnan, B. G. Reichl, T. Rosati, B. L. Samuels, A. Shao, R. Stouffer, M. Winton, A. T. Wittenberg, B. Xiang, N. Zadeh, R. Zhang, The GFDL global ocean and sea ice model OM4.0: Model description and simulation features. *J. Adv. Model. Earth Syst.* **11**, 3167–3211 (2019).

27. L. M. Harris, S.-J. Lin, C. Y. Tu, High-resolution climate simulations using GFDL HiRAM with a stretched global grid. *J. Climate* **29**, 4293–4314 (2016).

ScienceAdvances

Substantial global influence of anthropogenic aerosols on tropical cyclones over the past 40 years

Hiroyuki Murakami

View the article online
https://www.science.org/doi/10.1126/sciadv.abn9493
Permissions
https://www.science.org/help/reprints-and-permissions

Use of this article is subject to the Terms of service